

Enhanced Charge-Density-Wave Order and Suppressed Superconductivity in Intercalated Bulk NbSe₂

Huanhuan Shi^{1*}, Qili Li², Antoine M. T. Baron^{1,3}, Marie-Aude Méasson³, Sangjun Kang^{4,5,6}, Dirk Fuchs¹, Fabian Henssler¹, Alexander Haas², Paolo Battistoni¹, Nour Marayta¹, Michael Merz^{1,6}, Amir-Abbas Haghhighirad¹, Wulf Wulfhekel^{1,2}, Christian Kübel^{4,5,6}, Matthieu Le Tacon^{1*}

¹Institute for Quantum Materials and Technologies, Karlsruhe Institute of Technology, Kaiserstr. 12, 76131, Karlsruhe, Germany.

²Physikalisches Institut, Karlsruhe Institute of Technology, Wolfgang-Gaede-Str. 1, 76131, Karlsruhe, Germany.

³Institut Néel CNRS/UGA UPR2940, Rue des Martyrs 25, 38042, Grenoble, France.

⁴Institute of Nanotechnology, Karlsruhe Institute of Technology, Kaiserstr. 12, 76131, Karlsruhe, Germany.

⁵In-situ Electron Microscopy, Department of Materials and Earth Sciences, Technische Universität Darmstadt, Karolinengr. 5, 64289, Darmstadt, Germany.

⁶Karlsruhe Nano Micro Facility (KNMF), Karlsruhe Institute of Technology, Kaiserstr. 12, 76131 Karlsruhe, Germany.

*Corresponding author(s). E-mail(s): matthieu.letacon@kit.edu;
huanhuan.shi@kit.edu;

Abstract

The electronic ground states of transition-metal dichalcogenides are strongly shaped by reduced dimensionality, yet the properties of atomically thin layers remain difficult to probe due to their small size and environmental sensitivity. Here we demonstrate that controlled electrochemical intercalation of organic cations provides a robust bulk platform for accessing monolayer-like physics in NbSe₂. Intercalation of tetrapropylammonium and tetrabutylammonium expands the interlayer spacing by nearly a factor of two, electronically decoupling the NbSe₂ layers while simultaneously introducing well-defined charge doping. Using a combination of Raman spectroscopy, scanning tunneling microscopy, X-ray diffraction, and photoemission,

we uncover a pronounced enhancement of the charge–density–wave transition temperature to ~ 130 K together with a strong suppression of superconductivity, reproducing the phase diagram observed in exfoliated monolayers. The enhanced charge–density–wave order and reduced T_c arise from the combined effects of dimensionality reduction and electron injection, and are accompanied by distinct dip–hump anomalies in the tunneling spectra suggestive of collective mode excitations. Our results establish molecular intercalation as a powerful and scalable route for engineering competing orders in layered quantum materials.

Introduction

The reduced dimensionality of monolayer transition-metal dichalcogenides (TMDs) gives rise to distinctive physical properties absent in bulk crystals, spurring intense research activity in the field of low-dimensional materials [1, 2]. At the monolayer limit, direct band gaps in the visible range, strong spin–orbit coupling, and pronounced excitonic effects emerge, enabling phenomena and applications that are inaccessible in the bulk compound.

Bulk TMD 2H-NbSe₂ possesses a hexagonal $P6_3/mmc$ structure and hosts both a charge–density–wave (CDW) order and superconductivity, emerging below $T_{\text{CDW}} = 33$ K and $T_c = 7.2$ K, respectively. The interplay between these two orders has been extensively investigated [3–6]. Beyond its rich phase diagram, 2H-NbSe₂ serves as a model system to study CDW formation in dimensions $d > 1$, where the canonical Peierls picture of Fermi-surface-nesting–driven CDWs breaks down. Instead, the nearly commensurate instability at $q_{\text{CDW}} = (0.329, 0, 0)$ [7], responsible for the characteristic $\sim 3 \times 3$ superstructure, was shown to originate from anisotropic electron–phonon coupling [8, 9]. The superconductivity in this material is also believed to be conventional in nature [10], arising from the same electron–phonon interaction [3], making NbSe₂ a valuable platform for exploring the microscopic coupling between CDW and superconducting states.

A particularly appealing aspect of NbSe₂ is its tunability. External pressure [3, 11–13], strain [14], structural modifications such as misfit phases [15–17], and, most prominently, reduction in dimensionality to the monolayer limit [18, 19], all strongly reshape the balance between CDW and superconductivity, offering important insights into their microscopic origin.

The monolayer NbSe₂ prepared by mechanical exfoliation provides an ideal platform for examining these competing orders in the two-dimensional limit [20, 21]. Owing to its non-centrosymmetric structure and strong spin-orbit coupling, monolayer NbSe₂ hosts Ising superconductivity, a phenomenon absent in the bulk [22]. In this regime, T_c is strongly reduced to 0.9–3.7 K, while T_{CDW} increases rapidly, reaching 145 K [19]. In particular, this enhancement occurs without a change in the CDW wave vector [18, 23]. The opposing evolution of T_c and T_{CDW} reinforces the competitive relationship between CDW formation and superconductivity. Nevertheless, the microscopic mechanisms driving CDW order and superconductivity [24, 25], and the origins of their interplay [3, 9, 13, 26], remain the subject of active debate.

Despite their utility, exfoliated monolayers suffer from intrinsic limitations, including micron-scale lateral dimensions, time-consuming preparation, and air sensitivity, which restrict the range of experimental probes that can be reliably applied. To circumvent these challenges, chemical intercalation has emerged as an effective strategy to suppress interlayer coupling in bulk crystals and induce monolayer-like behavior without the need for exfoliation [27]. Beyond decoupling layers, intercalated ions can donate charge carriers, providing simultaneous control over dimensionality and electron density [28].

This approach has recently been brought to bear on NbSe₂. For example, Zhang *et al.* demonstrated that ionic-liquid intercalation results in a suppressed $T_{CDW} \approx 68$ K and enhanced $T_c \approx 6.9$ K compared to monolayer samples [29]. Similarly, tetraheptylammonium-intercalated NbSe₂ exhibits $T_{CDW} = 65$ K and $T_c = 7.1$ K [30]. These observations further support the competitive nature of CDW and superconductivity. However, intercalated NbSe₂ has not yet displayed the concurrent enhancement of T_{CDW} and suppression of T_c that is characteristic of the true monolayer limit.

In this work, we synthesize large-area (~ 1 mm) intercalated NbSe₂ crystals using variable-size organic cations (tetrapropylammonium (TPA⁺) and tetrabutylammonium (TBA⁺)) to systematically tune the interlayer spacing and carrier concentration. X-ray diffraction (XRD) and high-angle annular dark-field scanning transmission electron microscopy (HAADF-STEM) confirm that intercalation expands the interlayer spacing from 0.62 nm in the bulk to 1.22 nm in (TPA)_yNbSe₂ and

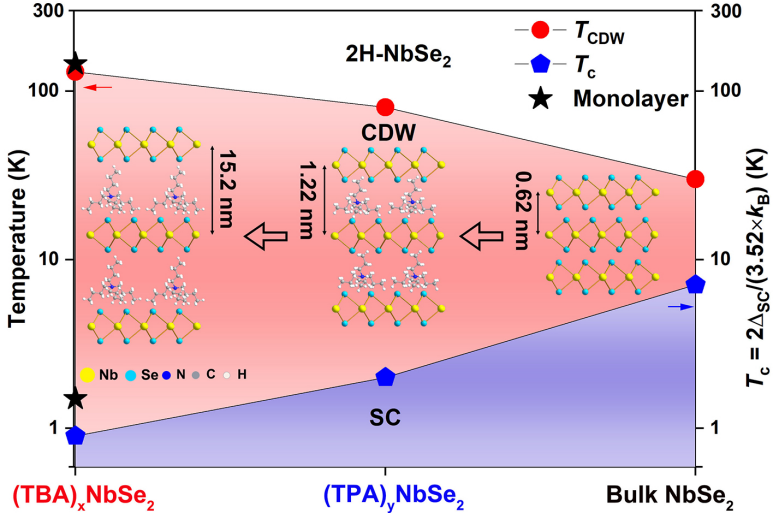


Fig. 1 Intercalant–temperature phase diagram of 2H-NbSe₂ based on Raman spectroscopy (T_{CDW}) and STM (from Δ_{SC} , see text); monolayer values are taken from Ref. [19].

1.52 nm in $(\text{TBA})_x\text{NbSe}_2$, effectively decoupling adjacent layers. Raman spectroscopy reveals a pronounced enhancement of T_{CDW} to 70 K in $(\text{TPA})_y\text{NbSe}_2$ and a record-high 130 K in $(\text{TBA})_x\text{NbSe}_2$, while scanning tunneling microscopy (STM) shows a strong suppression of the superconducting gap (Δ_{SC}), corresponding to reduced T_c values of 2 K and 0.9 K, respectively (Fig. 1). Notably, $(\text{TBA})_x\text{NbSe}_2$ exhibits behaviors closely resembling those of exfoliated monolayers. These results further support the intrinsic competition between CDW formation and superconductivity in NbSe₂ and establish molecular intercalation as a powerful route to access monolayer-like physics in bulk crystals.

Results

The structural effects of molecular intercalation (detailed in the Methods section) were investigated using a combination of Raman spectroscopy, XRD, and TEM. Reference Raman spectra obtained from pristine 2H-NbSe₂ single crystals are presented in Supplementary Information (Fig. S6) and exhibit all characteristic phonon modes previously reported at room temperature for this material. These include the A_{1g} mode (out-of-plane vibrations) at 234 cm^{-1} , the E_{2g}^1 mode (in-plane vibrations) at 250 cm^{-1} , the soft mode (associated with a second-order scattering process) at 181 cm^{-1} ,

and the E_{2g}^2 shear mode at 30 cm^{-1} . These features are well established in the literature for bulk NbSe_2 [31].

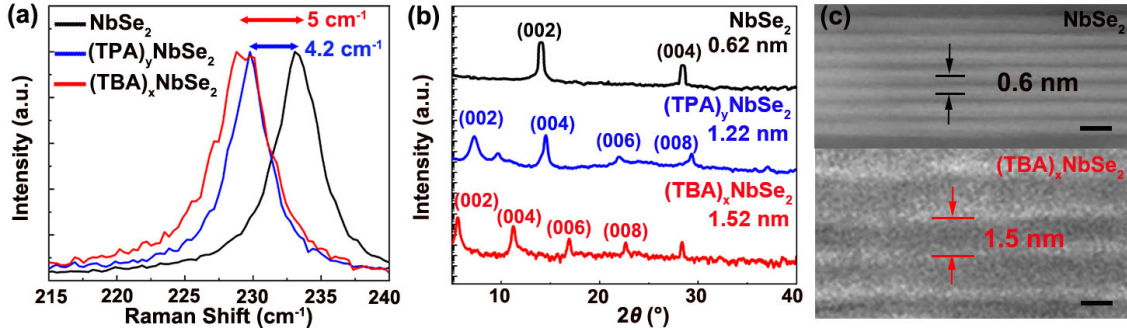


Fig. 2 (a) A_{1g} mode of NbSe_2 , $(\text{TPA})_y\text{NbSe}_2$ and $(\text{TBA})_x\text{NbSe}_2$; (b) XRD patterns of NbSe_2 , $(\text{TPA})_y\text{NbSe}_2$ and $(\text{TBA})_x\text{NbSe}_2$; (c) Cross-sectional HAADF-STEM images of pristine NbSe_2 (top) and intercalated $(\text{TBA})_x\text{NbSe}_2$ (bottom). Scale bars, 1 nm.

A direct signature of intercalation is shown in Fig. 2-a, where a systematic redshift of the A_{1g} mode is observed in the intercalated compounds (see full spectra in Supplementary Information Fig. S7). Notably, the phonon lineshape remains similar to that of the pristine sample, indicating good structural integrity after intercalation. Relative to pristine 2H- NbSe_2 , the A_{1g} mode softens by 4.2 cm^{-1} in $(\text{TPA})_y\text{NbSe}_2$ and by 5 cm^{-1} in $(\text{TBA})_x\text{NbSe}_2$, consistent with lattice expansion along the c -axis. The additional 0.8 cm^{-1} redshift observed in $(\text{TBA})_x\text{NbSe}_2$ relative to $(\text{TPA})_y\text{NbSe}_2$ suggests that the larger TBA^+ cation is more effective in weakening interlayer coupling in NbSe_2 .

More importantly, a substantial hardening of 9 cm^{-1} in the E_{2g}^1 mode, as well as a complete suppression of the shear mode, is observed in the intercalated samples. These behaviors closely mirror those of the monolayer NbSe_2 [19, 32]. Taken together, these results strongly suggest that the intercalated compounds effectively replicate the physical characteristics of the monolayer NbSe_2 .

Building on the Raman evidence for weakened interlayer coupling, we turn to XRD and cross-sectional TEM to quantitatively determine the interlayer separation and confirm the configuration adopted by the intercalated species. Indeed, tetraalkylammonium (TAA $^+$) ions can exist in two

primary configurations: a flattened form and a tetrahedral form (see Supplementary Information Fig. S8) [33]. Fig. 2-b compares the XRD patterns of the pristine and intercalated samples. The pristine crystal NbSe_2 exhibits sharp diffraction peaks (00ℓ) , corresponding to an interlayer spacing of 0.62 nm, in agreement with previous reports [30]. Upon intercalation, the (00ℓ) reflections of the pristine NbSe_2 disappear entirely, and a new set of (00ℓ) peaks appears at lower 2θ angles in the intercalated NbSe_2 , indicating successful intercalation of TAA^+ into the bulk crystal. According to XRD results, the interlayer distances of $(\text{TPA})_y\text{NbSe}_2$ and $(\text{TBA})_x\text{NbSe}_2$ are 1.22 nm and 1.52 nm respectively. Compared to pristine NbSe_2 , the interlayer distances expand by approximately 0.6 nm for $(\text{TPA})_y\text{NbSe}_2$ and 0.9 nm for $(\text{TBA})_x\text{NbSe}_2$. Notably, the expansion of $(\text{TPA})_y\text{NbSe}_2$ is larger than a flattened form (0.4 nm) but smaller than a tetrahedral form (0.78 nm) of TPA^+ , suggesting the presence of a distorted tetrahedral configuration of TPA^+ . In contrast, the expanded interlayer spacing observed for $(\text{TBA})_x\text{NbSe}_2$ is in good agreement with the tetrahedral TBA^+ cation, providing strong evidence that intercalation occurs by insertion of a single TBA^+ ion into its tetrahedral conformation (Fig. 1). This conformation is further corroborated by cross-sectional HAADF-STEM imaging (Fig. 2-c and Supplementary Information Fig. S9), which reveals an ordered lamellar structure with a periodicity in agreement with the XRD analysis.

Having determined both the conformation of the intercalated TAA^+ cations and the associated lattice expansion, we now turn to the effect of intercalation on the CDW properties of NbSe_2 . Fig 3 and Fig. S10 present temperature-dependent Raman spectra of pristine and intercalated NbSe_2 measured between 10 K and 290 K. The *ab* polarization configuration was used to minimize the background of elastic scattering, and all spectra were corrected for by the temperature-dependent Bose factor [34].

In pristine NbSe_2 , the soft mode redshifts upon cooling and saturates at 117.8 cm^{-1} below the CDW transition temperature $T_{\text{CDW}} = 33\text{ K}$ (Fig. 3-a). At lower temperatures, two additional Raman modes emerge at 28 cm^{-1} (amplitude mode) and 189 cm^{-1} , signaling the onset of CDW order, consistent with previous reports [35–37]. Strikingly, these CDW-associated modes appear

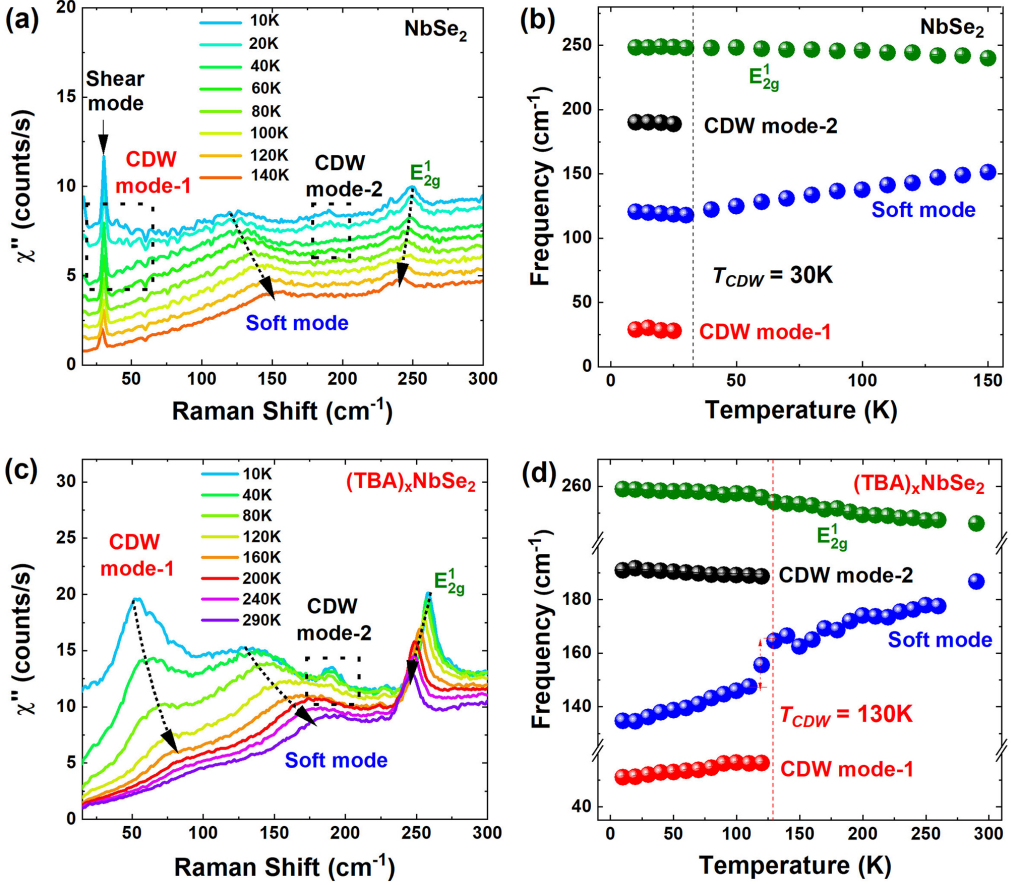


Fig. 3 (a,c) Temperature-dependent Raman spectra of pristine NbSe_2 (a) and intercalated $(\text{TBA})_x\text{NbSe}_2$ (c) in the ab polarization configuration; (b,d) Temperature dependence of the phonon frequencies in pristine NbSe_2 (b) and intercalated $(\text{TBA})_x\text{NbSe}_2$ (d).

at significantly higher temperatures in intercalated NbSe_2 (Fig. 3-c and Supplementary Information Fig. S10). The high-frequency mode remains near 189 cm^{-1} , while the amplitude mode blue-shifts to 60 cm^{-1} in $(\text{TPA})_y\text{NbSe}_2$ and 56 cm^{-1} in $(\text{TBA})_x\text{NbSe}_2$, reflecting enhanced electron–phonon coupling [19]. In particular, the amplitude mode in $(\text{TBA})_x\text{NbSe}_2$ can survive to higher temperatures than in $(\text{TPA})_y\text{NbSe}_2$.

To quantitatively extract T_{CDW} , the spectra were fitted using a damped harmonic oscillator model (see Supplementary Information Fig. S11-12) [38]. As shown in Fig. 3-b, the soft mode in pristine NbSe_2 softens from 181 to 118 cm^{-1} upon cooling to T_{CDW} , below which it stabilizes. A

similar trend is observed in $(TBA)_x\text{NbSe}_2$: the soft mode frequency follows a bulk-like behavior to 130 K, at which point it abruptly changes from 164.4 cm^{-1} to 147.5 cm^{-1} . This discontinuity is accompanied by anomalies in the A_{1g} and E_{2g}^1 phonon modes (see Supplementary Information Figs. S13-15). Concurrently, CDW modes emerge, gain intensity, harden and sharpen below 130 K, marking the onset of CDW order. These results clearly identify $T_{\text{CDW}} \approx 130\text{ K}$ in $(TBA)_x\text{NbSe}_2$, showing the highest reported T_{CDW} in intercalated NbSe_2 to date [29, 30].

To directly visualize the CDW order in real space, we performed STM measurements on $(TBA)_x\text{NbSe}_2$. Fig. 4-a displays representative STM topographs together with their two-dimensional Fourier transforms. A nearly perfect hexagonal atomic lattice is resolved, along with a well-defined, long-range incommensurate ($\sim 3 \times 3$) CDW modulation. In contrast to metal-intercalated NbSe_2 , where defects and disorder are often introduced [39], intercalation with TBA^+ produces no observable structural defects (see Supplementary Information Fig. S17) and preserves the integrity of CDW. The unit cell of the superlattice closely resembles that of pristine NbSe_2 [4], attesting to the minimal perturbation of the host lattice by the organic cation. Furthermore, compared to NbSe_2 , a wide CDW gap (Δ_{CDW}) of about 24 meV emerges near the Fermi level in $(TBA)_x\text{NbSe}_2$ (Fig. 4-b). That may be caused by partial Fermi surface gapping, multiband effects, and strong coupling mechanisms [18, 40]. Using the measured CDW gap ($\Delta_{\text{CDW}} \approx 24\text{ meV}$), we obtain

$$\frac{2\Delta_{\text{CDW}}}{k_{\text{B}}T_{\text{CDW}}} \approx 4.4,$$

exceeding the canonical weak-coupling BCS/Peierls value of 3.52 [41]. This elevated ratio is a hallmark of strong electron–phonon coupling and is often associated with CDW states that deviate from a simple nesting–driven Peierls picture, consistent with prior reports on NbSe_2 [39, 42].

In addition, we investigated the effect of cation intercalation on superconductivity using both STM and Raman spectroscopy. The STM measurements clearly show a well-defined Δ_{SC} of approximately 0.31 meV for $(\text{TPA})_y\text{NbSe}_2$ and 0.13 meV for $(TBA)_x\text{NbSe}_2$ (Fig. 4-c), which is about an order of magnitude smaller than gap sizes (1.1 meV) in the pristine NbSe_2 [4]. Assuming the weak coupling limit of BCS, the superconducting T_c is around 2 K for $(\text{TPA})_y\text{NbSe}_2$ and 0.9 K for

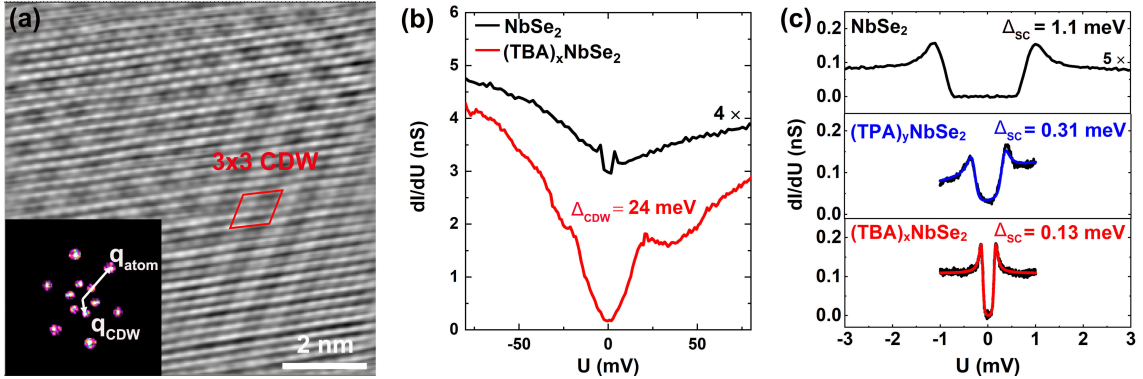


Fig. 4 (a) The STM image of the intercalated $(\text{TBA})_x\text{NbSe}_2$. The tip was stabled at sample bias 20 mV with tunneling current 20 pA; (b-c) CDW gap and superconductivity gap of NbSe_2 and intercalated $(\text{TBA})_x\text{NbSe}_2$ measured at 44 mK. Measuring conditions: (a) the tip was stabled at sample bias 20 mV with tunneling current 20 pA; (b) the tip was stabled at sample bias 100 mV and tunneling current 100 pA, and the lock-in amplifier had a modulation amplitude 4 mV; (c) the tip was stabled at sample bias 5 mV and tunneling current 100 pA with modulation amplitude 50 μV for NbSe_2 , and sample bias 1 mV and tunneling current 100 pA with modulation amplitude 15 μV for $(\text{TPA})_y\text{NbSe}_2$ and $(\text{TBA})_x\text{NbSe}_2$.

$(\text{TBA})_x\text{NbSe}_2$, respectively, indicating a strong suppression induced by cation intercalation. This suppression is in agreement with Raman data measured down to 2 K which shows no signature of superconductivity in $(\text{TBA})_x\text{NbSe}_2$. Indeed, the sharp superconducting mode that appears near 19 cm^{-1} in both *aa* and *ab* polarizations in pristine NbSe_2 [36] is completely absent in $(\text{TBA})_x\text{NbSe}_2$ (see Supplementary Information Fig. S18).

Discussion

The strong suppression of T_c observed in intercalated compounds may result from significant changes in carrier concentration introduced during the electrochemical process. The nominal electron density is estimated to be $\sim 2.1 \times 10^{14} \text{ cm}^{-2}$ (see Supplementary Information for details), corresponding to about 10% of the intrinsic carrier density in pristine NbSe_2 [43]. This is consistent with several independent spectroscopic signatures, including the shift of the density-of-states peaks toward negative bias in STM measurements and the redshift of the Nb 3d and Se 3d core levels (see Supplementary Information Figs. S19–S20), both of which indicate electron injection into the NbSe_2 layers.

Interestingly, larger electron doping achieved in NbSe_2 bilayers through misfit phases has recently been shown to suppress the CDW instability [17]. The contrast with our observations raises the question of whether the distinct behavior originates from the different doping amplitudes, or instead reflects qualitatively different responses in monolayers and bilayers. Addressing these possibilities will be an important direction for future study.

Further insight into the superconducting state is provided by the tunneling spectra, which display pronounced dip–hump anomalies at both positive and negative bias beyond the superconducting gap (see Supplementary Information Fig. S21). These features appear at an energy scale compatible with interband Josephson coupling and closely resemble the signatures recently associated with Leggett collective modes in single-layer NbSe_2 [44, 45]. While a definitive identification will require momentum-resolved probes and theoretical modeling, the similarity in phenomenology lends support to this interpretation. More broadly, these results underscore the potential of intercalated bulk crystals as a platform for exploring collective excitations in multiband superconductors.

Conclusion

In summary, we have shown that electrochemical intercalation of TPA^+ and TBA^+ ions into bulk NbSe_2 produces a substantial expansion of the interlayer spacing and an effective electronic decoupling of the constituent layers. This structural modification leads to a pronounced enhancement of the CDW transition temperature, reaching $T_{\text{CDW}} \simeq 130$ K, together with a strong suppression of superconductivity. The resulting phase diagram closely mirrors that of exfoliated monolayers [29, 46], demonstrating that molecular intercalation provides a robust and scalable route for accessing monolayer-like electronic ground states in macroscopic bulk crystals.

The concurrent enhancement of CDW order and reduction of T_c highlight the intrinsic competition between these two collective phenomena in NbSe_2 . Notably, the magnitude of the effects observed here exceeds that reported in mechanically exfoliated monolayers, suggesting that intercalation introduces additional tuning parameters—most prominently electron doping—that further

reinforce CDW order. The quantitative determination of the carrier density, supported by XPS and STM measurements, confirms the important role played by charge transfer in steering the balance between competing ground states.

Finally, the observation of dip–hump anomalies consistent with Leggett-mode–like collective excitations reveals new opportunities to investigate multiband dynamics and superconducting collective modes in the two-dimensional limit. Overall, molecular intercalation establishes a powerful platform for engineering dimensionality, carrier concentration, and competing orders in layered quantum materials, offering a promising pathway toward unraveling the microscopic mechanisms that govern unconventional charge-ordered superconductors.

Methods and Materials

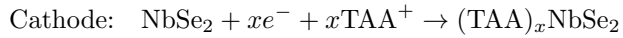
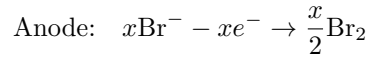
Synthesis of NbSe_2 single crystal

NbSe_2 Single crystals were grown by chemical vapour transport (CVT) using iodine (99.8 %, Riedel de Haën) as the transport agent. A mixture consisting of 2 g prereacted NbSe_2 , 120 mg of iodine and an additional 11.5 mg of selenium (99.9 %, Roth) was sealed under vacuum in a fused silicon ampoule. The ampoule was then placed in a two-zone furnace, with the source and sink temperatures maintained at 810 °C and 750 °C, respectively, to facilitate directed transport. After 12 days of growth under these conditions, large plate-shaped NbSe_2 crystals were obtained at the cooler end of the ampoule. Single crystals were achieved by washing with ethanol to remove iodine remains (see Supplementary Information Figs. S2-3).

Intercalation of $(\text{TAA})_x$ molecules

The intercalated NbSe_2 crystals were synthesized via an electrochemical intercalation process using a two-electrode system [47, 48] (see Supplementary Information Figs. S4), where the NbSe_2 crystal acted as cathode and a platinum foil was used as anode. The cathode and anode were placed in parallel with a constant distance of 1.0 cm. The electrolyte was made of tetraalkylammonium bromide (referred to hereafter as TAA^+ , alkyl = propyl, butyl) and anhydrous dimethylformamide

(DMF, 0.01 M, 5 mL). With a low current (20-80 μ A), organic cations such as TPA^+ and TBA^+ are capable of intercalating in van der Waals gaps of the NbSe_2 crystal (see Supplementary Information Fig. S4). By varying in size, the intercalated cations enable control over interlayer spacing and doping levels, making them a valuable tool to tune the electronic properties of NbSe_2 . The associated electrochemical reactions are outlined in the following equations:



The compositions of the intercalated crystals were determined to be $(\text{TPA})_{0.13}\text{NbSe}_2$ and $(\text{TBA})_{0.22}\text{NbSe}_2$ based on the number of transferred electrons and energy-dispersive X-ray spectroscopy (see Supplementary Information Section I, Table S1 and Figs. S1, S5 and S16). We could further check that the intercalated NbSe_2 samples remain stable for at least two months (see Supplementary Information Fig. S22), in contrast to the monolayer counterpart, which degrades within only a few hours [49].

Low-temperature Raman spectroscopy

Polarized Raman scattering was performed using a Horiba Jobin-Yvon LabRAM HR Evolution spectrometer equipped with a liquid-nitrogen-cooled CCD detector for measurements from 10 to 290 K. A He-Ne laser ($\lambda = 632.8$ nm) with power kept below 1 mW was focused on the sample through a $50\times$ objective, producing a spot size of $\sim 5\ \mu\text{m}$. To suppress elastically scattered light, the detection path included one notch filter and two Bragg filters. Spectra were acquired using $1800\ \text{mm}^{-1}$ and $600\ \text{mm}^{-1}$ gratings, corresponding to spectral resolutions of $0.6\ \text{cm}^{-1}$ and $1.6\ \text{cm}^{-1}$, respectively. Superconductivity mode was investigated using Trivista triple-grating Raman spectrometer with an incident laser line at 532 nm. Measurements were taken at 2 K with a ^4He

closed-cycle cryostat and and with low power (0.05 mW) to reduce laser heating effect. All spectra were corrected from the Bose thermal population factor.

To probe excitations of different symmetries, we employed two polarization configurations: parallel (*aa*) and perpendicular (*ab*), in which the incident light polarization lies along the crystallographic *a* axis and is either parallel or perpendicular to the polarization of the scattered light, respectively. According to Raman selection rules [50], these geometries allow access to the A_{1g} + E_{2g} and E_{2g} symmetry channels, respectively, in the hexagonal phase (point group D_{6h}^1).

Scanning tunneling microscopy

STM measurements were performed in a home-built ultra-high vacuum chamber housing a slider-type STM at milli-Kelvin temperatures [51]. The base pressure during the experiments was 1×10^{-10} mbar. The intercalated NbSe_2 was cleaved under ultrahigh vacuum with Kapton tape at room temperature and then immediately transferred to STM. All STM images were recorded in constant current mode. The W tip was initially prepared by flashing in the preparation chamber and was controlled in STM by dipping it into an Au(111) substrate, as well as by voltage pulsing on NbSe_2 . A lock-in amplifier was used for spectroscopy.

References

- [1] S. Manzeli, D. Ovchinnikov, D. Pasquier, O. V. Yazyev, and A. Kis, *Nat. Rev. Mater.* **2**, 17033 (2017).
- [2] Q. Wang, K. Kalantar-Zadeh, A. Kis, J. N. Coleman, and M. S. Strano, *Nat. Nanotechnol.* **7**, 699 (2012).
- [3] M. Leroux *et al.*, *Phys. Rev. B* **92**, 140303 (2015).
- [4] A. Sanna *et al.*, *npj Quantum Mater.* **7**, 6 (2022).
- [5] K. Cho *et al.*, *Nat. Commun.* **9**, 2796 (2018).
- [6] A. Majumdar *et al.*, *Phys. Rev. Mater.* **4**, 084005 (2020).
- [7] D. E. Moncton, J. D. Axe, and F. J. DiSalvo, *Phys. Rev. Lett.* **34**, 734–737 (1975).
- [8] F. Weber *et al.*, *Phys. Rev. Lett.* **107**, 107403 (2011).
- [9] M. D. Johannes, I. I. Mazin, and C. A. Howells, *Phys. Rev. B* **73**, 205102 (2006).
- [10] T. Valla *et al.*, *Phys. Rev. Lett.* **92**, 086401 (2004).
- [11] C. Berthier, P. Molinie, and D. Jérôme, *Solid State Commun.* **18**, 1393 (1976).
- [12] H. Suderow, V. G. Tissen, J.-P. Brison, J. L. Martínez, and S. Vieira, *Phys. Rev. Lett.* **95**, 117006 (2005).
- [13] Y. Feng *et al.*, *Proc. Natl. Acad. Sci. U.S.A.* **109**, 7224 (2012).
- [14] S. Gao *et al.*, *Proc. Natl. Acad. Sci. U.S.A.* **115**, 6986 (2018).
- [15] J. Rouxel, A. Meerschaut, and G. Wiegers, *J. Alloys Compd.* **229**, 144 (1995).

- [16] R. T. Leriche *et al.*, *Adv. Funct. Mater.* **31**, 2007706 (2021).
- [17] L. Zullo *et al.*, *Phys. Rev. B* **110**, 075430 (2024).
- [18] M. Ugeda *et al.*, *Nat. Phys.* **12**, 92 (2016).
- [19] X. Xi *et al.*, *Nat. Nanotechnol.* **10**, 765 (2015).
- [20] P. Baidya *et al.*, *Phys. Rev. B* **104**, 174510 (2021).
- [21] Y. Cao *et al.*, *Nano Lett.* **15**, 4914 (2015).
- [22] X. Xi *et al.*, *Nat. Phys.* **12**, 139 (2016).
- [23] Y. Nakata *et al.*, *npj 2D Mater. Appl.* **2**, 12 (2018).
- [24] F. Zheng and J. Feng, *Phys. Rev. B* **99**, 161119 (2019).
- [25] D. Wickramaratne, S. Khmelevskyi, D. F. Agterberg, and I. I. Mazin, *Phys. Rev. X* **10**, 041003 (2020).
- [26] O. Moulding, I. Osmond, F. Flicker, T. Muramatsu, and S. Friedemann, *Phys. Rev. Res.* **2**, 043392 (2020).
- [27] Z. Wan *et al.*, *Nature* **632**, 69 (2024).
- [28] M. S. Dresselhaus and G. Dresselhaus, *Adv. Phys.* **30**, 139 (1981).
- [29] H. Zhang *et al.*, *Nat. Phys.* **18**, 1425 (2022).
- [30] L. Yu *et al.*, *ACS Appl. Mater. Interfaces* **16**, 59049 (2024).
- [31] R. Grasset *et al.*, *Phys. Rev. B* **97**, 094502 (2018).
- [32] P. Tan *et al.*, *Nat. Mater.* **11**, 294 (2012).

[33] W. Roth *et al.*, J. Am. Chem. Soc. **143**, 11052 (2021).

[34] K. Sen *et al.*, Nat. Commun. **11**, 4270 (2020).

[35] J. C. Tsang, J. E. Smith, and M. W. Shafer, Phys. Rev. Lett. **37**, 1407 (1976).

[36] R. Sooryakumar and M. V. Klein, Phys. Rev. Lett. **45**, 660 (1980).

[37] M. A. Méasson *et al.*, Phys. Rev. B **89**, 060503 (2014).

[38] Z. Cao *et al.*, Phys. Rev. B **107**, 245125 (2023).

[39] U. Chatterjee *et al.*, Nat. Commun. **6**, 6 (2015).

[40] C. Wang, B. Giambattista, C. G. Slough, R. V. Coleman, and M. A. Subramanian, Phys. Rev. B **42**, 8890 (1990).

[41] J. Bardeen, L. N. Cooper, and J. R. Schrieffer, Phys. Rev. **108**, 1175 (1957).

[42] S. V. Borisenko *et al.*, Phys. Rev. Lett. **102**, 166402 (2009).

[43] X. Xi, H. Berger, L. Forró, J. Shan, and K. F. Mak, Phys. Rev. Lett. **117**, 106801 (2016).

[44] A. J. Leggett, Prog. Theor. Phys. **36**, 901 (1966).

[45] W. Wan *et al.*, Adv. Mater. **34**, 2206078 (2022).

[46] Y. Nakata *et al.*, Nat. Commun. **12**, 5873 (2021).

[47] H. Shi *et al.*, Angew. Chem. Int. Ed. **62**, e202303929 (2023).

[48] H. Shi *et al.*, Adv. Mater. **32**, 1907244 (2020).

[49] H. Wang *et al.*, Nat. Commun. **8**, 394 (2017).

- [50] W. Hayes and R. Loudon, *Scattering of Light by Crystals* (John Wiley and Sons, New York, 1978).
- [51] T. Balashov, M. Meyer, and W. Wulfhekel, Rev. Sci. Instrum. **89**, 113707 (2018).

Acknowledgements. H. Shi thanks S. Souliou, M. Frachet, and C. Singh for fruitful discussion and is grateful to the Karlsruhe Nano-Micro Facility (KNMFi) for technical support. We acknowledge the funding by the European Research Council (ERC) under the European Union’s Horizon 2020 research and innovation programme (Grant Agreement n° 865826), the Deutsche Forschungsgemeinschaft (DFG, German Research Foundation), Grant No. TRR 288-422213477 (Project B03, B06 and B10), Project No. 449386310 and CRC FLAIR.

Contributions. H.S. and M.L.T. conceived the project. H.S., F.H., P.B., A.B., M.A.M. and M.L.T. performed the polarized Raman scattering measurements and carried out the Raman data analysis. Q.L., A.H., and W.W. conducted the STM experiments. S.K. and C.K. performed the TEM experiments. D.F., N.M., and M.M. performed the XRD measurements. A.-A.H. grew the single crystals. H.S. synthesized the intercalated crystals. H.S. and M.L.T. wrote the manuscript with input from all authors.

Competing interests. The authors declare no competing interests.

Supplementary information. The online version contains supplementary material available at XXXXXX.